

Super Arrhenius temperature dependent viscosity due to liquid-liquid phase separation in the super-cooled Kob-Andersen model

Jayne Brickley and Xueyu Song

Department of Chemistry and Ames Laboratory ,

Iowa State University, Ames, IA 50011, USA

arXiv:2602.16060v1 [cond-mat.stat-mech] 17 Feb 2026

Abstract

In this paper, we introduce a new order parameter called the weighted coordination number (WCN) to study the liquid-liquid (LL) phase separation, using the temperature-dependent coarsening of the LL interface as a possible mechanism for the glass transition. The well-established glass-forming Kob-Andersen binary Lennard-Jones system is used for our studies. The gas-liquid binodal line is reconstructed using the WCNs, and the same approach is extended to study the liquid-liquid binodal line. Systems of various densities are instantaneously quenched from high to low temperatures where a liquid-liquid separation is observed. Densities and the composition of each liquid state are used to check the level rule, along with density and pressure profiles, demonstrating local equilibrium of liquid-liquid phase separation. The transition from the liquid-liquid phase separation in the supercooled region to the glass transition region is modeled by adopting a Markov Network Model to estimate the temperature dependent viscosity using liquid-liquid interfacial information from the classification.

I. INTRODUCTION

In two recent papers, a weighted coordination number of particles is used as an order parameter to characterize domains of a model supercooled liquid [1, 2]. The salient feature of such an order parameter is its ability to differentiate the structural features of macroscopic states in the structural space and at the same time the particles belonging to the different macroscopic states form intertwining domains in the configurational space by utilizing the particle's identity in both spaces. Using such an order parameter as a "classification indicator", we show that there is a clear liquid-liquid phase separation by measuring various thermodynamic and dynamic properties of the super-cooled Kob-Andersen model system. Our studies also show that these domains structure as a result of the liquid-liquid phase separation naturally lead to two types of relaxation dynamics; the intra-domain relaxation largely due to diffusion inside a domain, and the inter-domain relaxation, which is related to the coarsening kinetics of the first-order phase transition.

In the current contribution, the phase diagram of such a liquid-liquid(L-L) phase transition is calculated, including the positions of the critical point from the L-L transition and the liquid-gas transition. More importantly, by computing the temperature-dependent viscosity in the supercooled region it is found that the coarsening kinetics of the L-L transition may provide a convincing picture for the glass transition in this model system.

The paper is organized as follows. In the next section, our classification scheme, simulation

details and the phase diagram of the model system are presented. In section III, density and pressure profiles of the L-L transition are characterized and from these profiles the surface tensions in different regions of the interface are calculated. In section IV, using the surface tension of the system, a two-state Markov network model is used to calculate the temperature-dependent viscosity in the deep super-cooled region, which is shown to agree with the literature result. Some concluding remarks are presented in section V.

II. CLASSIFICATION SCHEME

A. Simulation Details

In this work, simulations are performed using the binary Kob-Andersen Lennard-Jones potential [3, 4]. This model is well known for its ability to avoid crystallization well below the melting temperature, making it an excellent model system for studying viscous liquids and the glass transition. Liquid-liquid separations have been observed in our previous study[2] using this potential in addition to glass transition studies via equation of state constructions [5, 6]. The Kob-Andersen model can be expressed as

$$V(r) = \begin{cases} 4\varepsilon_{A,B} \left[\left(\frac{\sigma_{A,B}}{r} \right)^{12} - \left(\frac{\sigma_{A,B}}{r} \right)^6 \right] & \text{for } (r \leq r_c) \\ 0 & \text{for } (r > r_c), \end{cases} \quad (1)$$

where ε is the energy well depth, σ is the atomic diameter and r_c is the cutoff radius (set to $2.5\sigma_{AB}$). The system consists of 80% type A particles and 20% type B particles, with parameters $\sigma_{BB}/\sigma_{AA} = 0.88$, $\sigma_{AB}/\sigma_{AA} = 0.8$, $\varepsilon_{BB}/\varepsilon_{AA} = 0.5$, and $\varepsilon_{AB}/\varepsilon_{AA} = 1.5$. The model is asymmetric to allow particles of type B to act as agitators, preventing the system from crystallizing. Systems are run under the NVT or NPT ensemble with periodic boundary conditions while using the Nose-Hoover thermostat and barostat. The parameters for solid Ar are chosen for unit conversion, with $\sigma = 0.3405\text{\AA}$, $m = 6.69 \times 10^{-26}\text{kg}$ and $\frac{\varepsilon}{k_B} = 119.8\text{K}$. The timestep is set to 0.005τ (12 femtoseconds), and system sizes include $N = [16000, 27000, 32000]$. The liquid is prepared at a temperature of $T^* = 1.2$, which is well above the mode-coupling temperature $T^* = 0.435$ at $\rho^* = 1.2$ estimated by mode-coupling theory [7], and allowed to relax for one million timesteps (12ns). Each system is then instantaneously quenched to the target temperature and equilibrated on the order of microseconds at lower temperatures, after which all relevant data is collected.

B. WCN as an order parameter for classification

It has previously been shown weighted coordination numbers (WCNs) accurately describe local structural and dynamic heterogeneities in supercooled liquids[1, 2]. In short, the method is based on the commonly employed coordination numbers (CNs) for normal liquids, with the addition of normalized Gaussian distributions at each notable solvation feature of the radial distribution function $g(r)$. Because the typical order parameters used to differentiate states of matter fail for phases where all thermodynamical variables are similar such as condensed amorphous states, a new type of order parameters is needed to accurately describes a particle's local environment to capture amorphous states' local structural differences. The highly averaged structural information given by $g(r)$ coupled with more detailed description of each particle's neighboring environment allows for a balanced compromise to group particles with similar structural features together. As a liquid state is decreased further in temperature, dynamical and spatial heterogeneities begin to arise and individual CNs of particles increase dramatically with the liquid state complexity. WCNs alleviates the issue of individual assignment for each particle, rather a statistical assignment with the solvation features based on $g(r)$. This method proves to be an excellent balance between the strict assignment of CNs of individual particles, which leads to many structurally different states, and the single structural state based on $g(r)$.

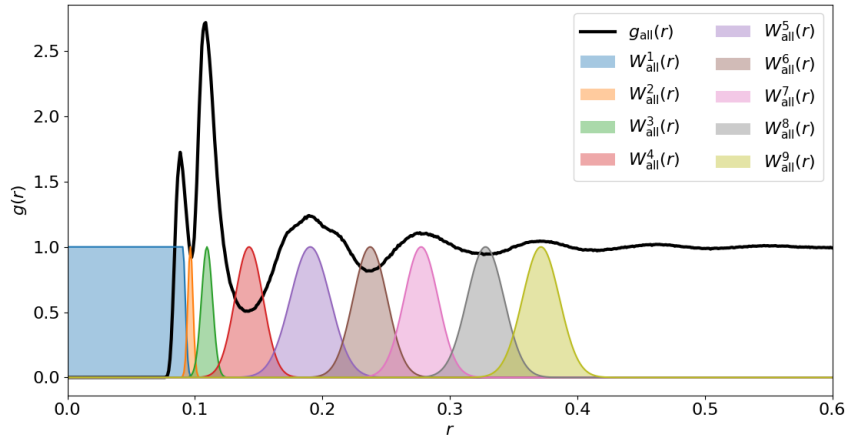


Fig. 1: The radial distribution function with weighted Gaussians placed at each notable feature for a KA binary LJ system at $T^* = 0.43$, $\rho^* = 1.12$. The Gaussian widths are chosen so the the height at the intersection points is below 0.25.

In this method, Gaussians are placed at the center of each feature of the $g(r)$ and an intersection



(a) 2D projection in PC space

(b) 2D projection in configuration space

Fig. 2: (a) 2D projection of PC space for KA binary LJ system at $T^* = 0.3$, $\rho^* = 1.12$.
(b) Corresponding 2D projection in configuration space using K-means clustering information from PC space.

tolerance of 0 to 0.25 is allowed for continuity of solvation shells. WCNs are treated as per-particle vectors with dimension equal to the number of features in $g(r)$, $N=9$ is shown in the Fig. 1. We have shown that the number of shells included in each WCN has no bearing on distinguishing the heterogeneities of the local structures once the major features of the $g(r)$ are captured, thus using more than 9 features won't change our results. A particle's WCN is constructed by assigning a value to each particle's solvation feature by counting its neighboring particles weighted by that feature's Gaussian distribution [1]. These values are then summed and averaged for each feature such that $\overline{WCN}_i = \frac{1}{N_b} \sum_j^{N_b} WCN_j$, where N_b is the number of neighboring particles j of particle i to obtain the final WCN of that particle after this further smoothing.

N features can then be represented by a matrix \mathbf{X} with dimension $M \times N$ for a system of M particles. Principle Component Analysis (PCA) is employed to reduce the number of features of \mathbf{X} , which are correlated, to a few highly correlated ones for presentation. PCA is a useful non-parametric dimensionality reduction tool used commonly in data analysis with the following procedure:

- a) Obtain the mean-free data of WCNs $\tilde{\mathbf{X}} = \mathbf{X} - \langle \mathbf{X} \rangle$, which is averaged over M particles for each WCN.
- b) Form the correlation matrix $C = \tilde{\mathbf{X}}^T \tilde{\mathbf{X}}$, which has the dimension $N \times N$.
- c) Solve the eigenvalue problem $Cu_i = \sigma_i^2 u_i$ to obtain the principle components u_i . All PCs are retained and used to form the basis \mathbf{U} , which is then dotted with the original dataset \mathbf{X} to obtain the new feature space data $Y = U^T X$, which is called PC space.

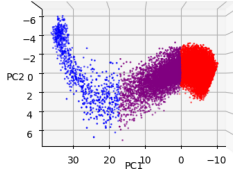
Although not required, PCA allows for a meaningful 3-dimensional view of the feature space.

It is important to note that the success of the classification does not depend on the N features being correlated. Systems of different morphologies often have distinct representations in PC space that allows for quick visual analysis of a system. This difference is most prominent in the arrangement of PCs of the KA gas and liquid states, seen in Fig. 3.

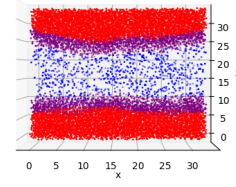
We then use K-means clustering to extract clustering information from the correlated features in the feature space, setting $k = 2$ with a priori knowledge that the system contains two distinct thermodynamic states (i.e. gas-liquid, liquid-liquid, etc), larger k values will converge to $k = 2$ after convergence test [1]. K-means is an unsupervised, geometric-based clustering algorithm that is excellent at distinguishing initial features in the PC space. The clustering information obtained by K-means can then be mapped from the PC space back to the real space given the identity of the particles. These clusters in the real space serve as the essential signature of observing a phase separation.

Depending on the thermal stability of the system interfacial particles must be treated with more care. Two different approaches are required to alleviate the hard assignment of interfacial particles from K-means in real space and feature space. For feature space, we employ the commonly used Gaussian Mixture Model which utilizes multivariate Gaussians and maximize log-likelihood for a softer assignment. In real space, we can tag interfacial particles and switch their cluster assignment, essentially allowing clusters to grow or shrink in size. This co-learning strategy is iterated upon until the number of particles that change assignment is less than 1% of the total system size, where the convergence is documented in Ref.[2]. Once converged, we may then gather relevant data for each cluster. Data can be collected for the density and pressure profiles using such an order parameter, and is shown that no significant difference in these profiles after convergence, hence this order parameter can be used to identify two thermodynamically different liquid states. The pressure and density profiles of our model system will be described in Sec.III.

It can be shown that the need for iterations to better define the interface of the liquid-liquid separation is dependent on the thermodynamics of the system. If thermal fluctuations are high, the need for iteratively defining the interface is unnecessary, as averages will be dominated thermally. For lower temperature near or below the glass transition, the lack of thermal fluctuations calls for a more precise definition of the liquid-liquid interface.



(a) WCNs in PC space for gas-liquid coexistence



(b) Gas-liquid coexistence in configurational space

Fig. 3: (a) 2D projection of PC space for KA binary LJ system at $T^* = 0.8$, $\rho^* = 0.5$ with interfacial particles. (b) 2D projection of configuration space using K-means clustering information from PC space with $k=3$ to visualize interfacial particles.

C. Phase Diagram

WCNs have the capability to distinguish any combination of states by characterizing small and large local structure differences, such as liquid-crystal [1], liquid-liquid [2] and liquid-gas. To demonstrate this, the well established gas-liquid binodal line for the Kob-Andersen model will be reconstructed and compared with those found in other literature [7]. The same strategy will be extended to the liquid-liquid binodal. Normally, liquid phases are indistinguishable from each other by conventional order parameters such as density. Therefore, the utility of WCN as an order parameter can be demonstrated by the construction of the gas-liquid and liquid-liquid phase diagram within the entire thermodynamic variable space.

The calculated Kob-Andersen gas-liquid binodal line using the WCN order parameter is compared with a literature one[7], which was constructed by using density as an order parameter in Fig. 5. Each system is equilibrated at $T^* = 2.0$ and quenched to target temperatures $T^* = \{1.15, 1.07, 1.0, 0.9, 0.8, 0.6\}$ with densities $\rho^* = \{0.4, 0.425, 0.445, 0.47, 0.5, 0.525\}$, respectively. After ten million time steps of equilibration, averaged WCNs are collected with 11 frames spaced over a nanosecond. Gas and liquid particles are easily classified due to the large difference in their local structures, driven by the density dependent $g(r)$. Fig. 3 demonstrates this for a planar interface at $T^* = 0.8$, $\rho^* = 0.5$. Gas and liquid state information obtained from the classification is used to obtain their average density for every system, which is then used to construct the gas-liquid binodal line. Not only can WCNs differentiate states from one another, but it can also be used to show interfacial particles for a well-defined interface between a gas-liquid

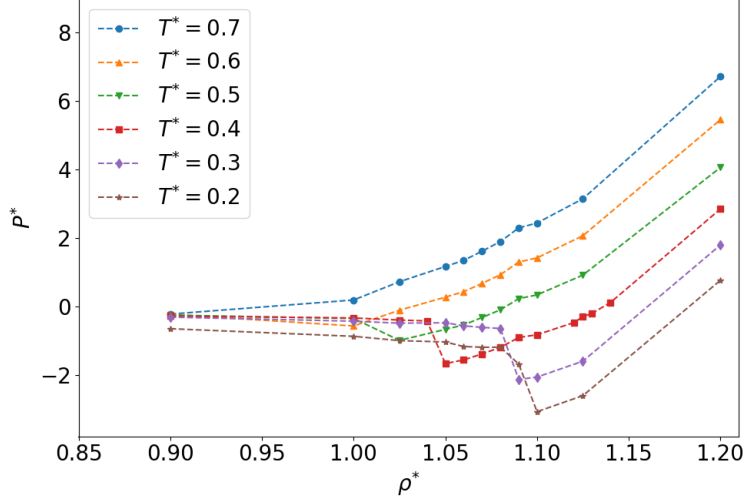


Fig. 4: Isotherms of the Kob-Andersen system. Monotonicity ends below $T^* = 0.6$, signifying a first-order phase transition from liquid-liquid metastability to liquid-liquid instability. Minima of non-monotonic isotherms, $\rho_s^*(T)$, represent densities in which gas nucleation ceases and liquid-liquid phase separation occurs.

coexistence.

Once the gas-liquid binodal line has been obtained, we then begin the construction of the liquid-liquid binodal line. To determine where the gas phase falls out of equilibrium upon quenching from $T^* = 1.2$, we compute isotherms to determine where the first-order phase transition from liquid-gas to liquid-liquid occurs. Restricted ensemble Monte-Carlo and empirical free energy methods used by Ref.[6] to estimate the gas-liquid spinodal line yields a lower density limit for gas phase instability. Once the gas phase falls out of equilibrium with the liquid phase, metastability of two liquid states is observed in Fig. 4. From our observations, there is competition in this region between gas formation and liquid-liquid separation. For isotherms $T^* \leq 0.5$, non-monotonicity is indicative of the liquid-gas to liquid-liquid transition. Bulk densities $\rho^* > 1.125$ result in no liquid-liquid formation within the given simulation limit. Similarly, points prior to non-monotonicity exhibit gas nucleation while cooling or during the $1.2\mu\text{s}$ of equilibration. Whether a liquid-liquid separation occurs prior to gas nucleation was not studied, but it could be the case. Further study in this region might possibly yield the transition from liquid-liquid to liquid and subsequently the entire Van der Waals style loop, which is beyond the scope of this study. The gas-liquid-liquid triple point was not observed in this study.

These densities from the isotherms then serve as a lower limit to start scanning for the liquid-

ρ_{bulk}^*	ρ_1^*	ρ_2^*	% State 1	% State 2
1.08	1.03	1.17	60	40
1.09	1.03	1.17	52	48
1.10	1.03	1.18	47	53
1.12	1.03	1.18	40	60

TABLE I: Table of quenched NVT systems at $T^* = 0.4$, demonstrating the lever rule for each sampled bulk density.

liquid phase transition while avoiding gas nucleation. By sampling various bulk densities and quenching to target temperatures, the liquid-liquid binodal line can be obtained by measuring the densities of classified states using WCNs. Densities of liquid states were obtained by finding large clusters of each state within the simulation box following the classification, selecting a volume deep within said clusters, and monitoring the number of particles that remained within over the course of the trajectory. Equilibration time for the sampled state points ranges from 50-300ns depending on the target temperature, and densities were averaged over 5ns. The percentage of each liquid state that makes up the simulation box, or χ_i , is used to check the lever rule at each bulk density, which is a stringent test for thermodynamic equilibrium. According to the lever rule, the density of the two liquid states should not change with the bulk density at a given temperature, only their partition within the system. Indeed, the ratio of the liquid states is in agreement with the bulk density (Table I). This procedure was carried out for $T^* = 0.3, 0.4$, and 0.5 .

By sampling various bulk densities and quenching to target temperatures, the liquid-liquid binodal line can be obtained by measuring the densities of classified states. Estimated liquid-liquid binodal line is shown in Fig. 5 and also tabulated in Table II. The critical point can be estimated using law of rectilinear diameters $(\rho_g + \rho_l)/2 = aT + b$ [8]. Namely, the critical density $\rho_c^* = 1.1$ is estimated based on the density data near the critical point. Using the three data points near the critical point, parameters from the fitting leads to $a = 0.92$, $b = 0.55$, hence the critical temperature $T_c^* = 0.6$.

III. DENSITY AND PRESSURE PROFILES

To demonstrate mechanical equilibrium along the rough interface of liquid-liquid separation, relatively large regions of positive and negative curvature must be thoroughly examined via

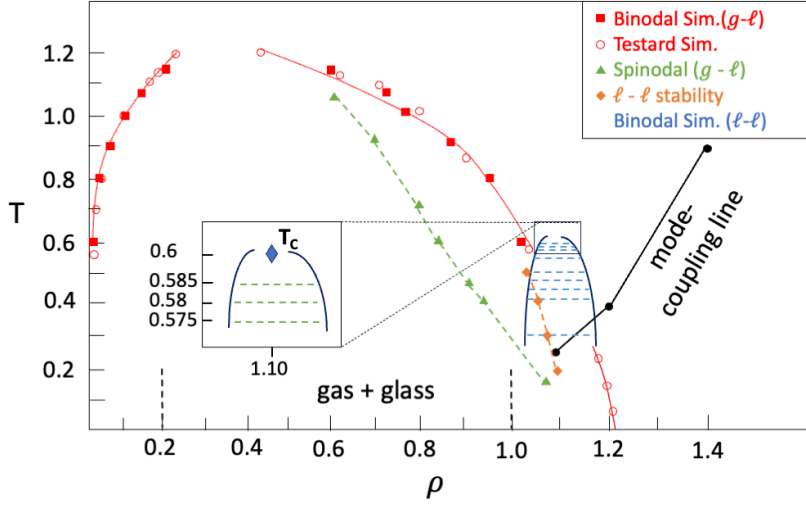


Fig. 5: Phase diagram of the KA binary LJ potential. All systems are equilibrated at $T^* = 2.0$ before instantaneously quenching to the target temperature. The bulk density for gas-liquid systems was varied to obtain ideal separations, targeting spherical liquid clusters when possible. States were identified using WCN classification, which is then used to obtain average densities over 5ns. Densities at which the liquid-liquid separation was examined include $T^* = \{0.3, 0.4, 0.43, 0.46, 0.5, 0.52, 0.55, 0.575, 0.58, 0.585\}$, and the lever rule was verified at key temperatures. Open circles are from [7] and filled squares are from our simulations. The blue curve is the liquid-liquid binodal line from our simulations with detailed data listed in Table II. The gas-liquid spinodal line (green), taken from ref [6], is estimated using Restricted Monte Carlo. Diamonds indicate end of gas nucleation and beginning of $l-l$ separation.

T^*	0.3	0.4	0.43	0.46	0.5	0.52	0.55	0.575	0.58	0.585
ρ_1^*	1.03	1.034	1.035	1.041	1.043	1.051	1.052	1.059	1.077	1.082
ρ_2^*	1.194	1.189	1.159	1.147	1.140	1.138	1.134	1.122	1.118	1.112

TABLE II: Binodal line of the liquid-liquid coexistence of the Kob-Andersen model. Systems are quenched to target temperatures from $T^* = 2.0$, all at bulk density $\rho^* = 1.09$. Each system is equilibrated for a minimum of 400ns or maximum of $1.8\mu s$ depending on T^* , with data collection occurring over 12ns. Vertical slices are taken over various regions in each simulation box and averaged, using small areas where state information is stagnant over the course of the trajectory.

pressure and density profiles to extract underlying thermodynamic properties. Systems of size $N=32000$ are equilibrated in the NPT ensemble at zero pressure, $T^* = 1.2$. The system is then quenched down to $T^* = 0.3$ and equilibrated for $1.5 \times 10^8 \tau$. Per-atom pressure tensors are obtained via LAMMPS [9] molecular dynamics package using its per-atom stress tensor. An appropriate spherical interfacial region is identified for the higher pressure state, and the six Cartesian stress tensor components are transformed into spherical coordinates with respect to the center of the

cluster. Due to the low magnitude of the off-diagonal terms, the pressure can be expressed as

$$P(r) = P_N(r)e_r e_r + P_T(r)(e_\theta e_\theta + e_\phi e_\phi), \quad (2)$$

where e_r , e_θ , e_ϕ are the spherical unit vectors. P_N and P_T are the normal and tangential pressure components, respectively. P_N and P_T are obtained via numerical average of pressure within of thin spherical shells extending out from each cluster center. This procedure is done for both types of curvature along the interface within the liquid-liquid separation domains. Density data are also collected over these same bins. Two different types of curvature exist across the liquid-liquid interface, convex(positive curvature) and concave(negative) regions. Both regions exhibit similar but different pressure and density profiles. Working from the lower pressure liquid state, density and pressure profiles can be obtained for both types of interfaces. The peculiar situation arises from the concave case, where negative curvature acts as destructive interference towards the total surface tension, wherein mechanical equilibrium is not maintained perfectly, an indication that the system is in a local equilibrium which leads to coarsening kinetics in a longer time scale [2].

Mechanical equilibrium is expressed as

$$P_T(r) = P_N(r) + \frac{r}{2} \frac{dP_N(r)}{dr}, \quad (3)$$

which satisfies the condition $\nabla \cdot \mathbf{P} = 0$ [10]. One of the challenges of studying these different curvature sections across an interface comes from the amount of available surface data, as the desired regions are rather small regardless of system size. Using the thin sheet approach, a given curved region of an interface may only have 40 to 50 particles per sampled shell, making statistically accurate averaging in these regions difficult.

To ensure the proper sampling, within the given time interval block averages can be taken for each bin of particles [11]. Block averaging is a common statistical analysis technique that ensures data after a certain time t are uncorrelated. The obtained pressure and density profiles paint a unique picture of a phase separation that maintains mechanical equilibrium. The results obtained for the convex case (Fig. 6) mimic results found in most other convex fluid systems [12], however the concave pressure profile is uniquely different and minutely breaks mechanical equilibrium. Data for the concave case was studied at two temperatures, $T^* = 0.2, 0.3$, which both show the same qualitative behaviors. Both the density and pressure profiles in the concave case (Fig. 7) see

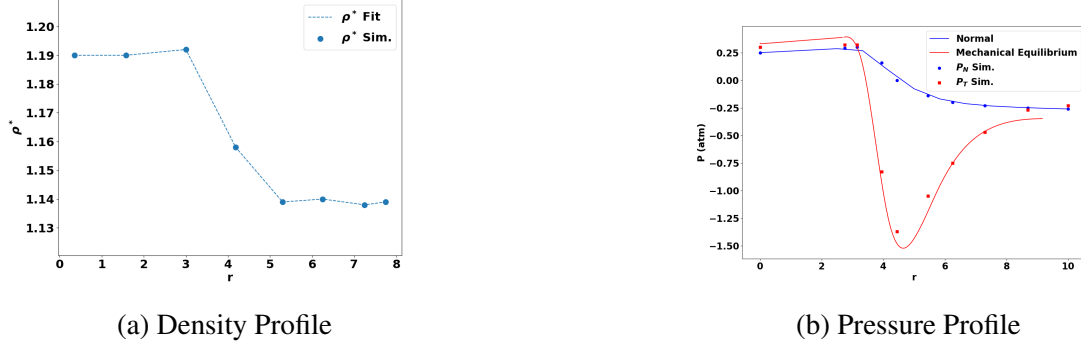


Fig. 6: (a) Density profile and (b) pressure profile of $T^* = 0.3$, $\rho^* = 1.17$. NPT system at zero pressure for convex region of the liquid-liquid interface. The surface of tension lies at $R_s = 3.94$ (Table III). Error for each data point $< 0.01 \text{ atm}$.

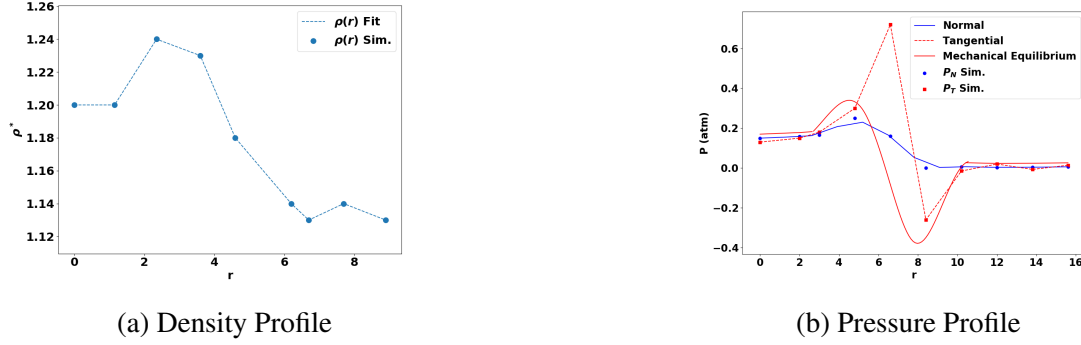


Fig. 7: (a) Density profile and (b) pressure profile of $T^* = 0.3$, $\rho^* = 1.17$. NPT system at zero pressure for concave region of the liquid-liquid interface. The surface of tension lies at $R_s = 3.84$ (Table III). Error for each data point $< 0.009 \text{ atm}$.

an increase in ρ and P_N shortly before the surface of tension. This suggests local inhomogeneity along these regions of the liquid-liquid interface, and the breaking of mechanical equilibrium provides a driving force for interface evolution at longer time scales.

We can integrate the pressure and density profiles of the two curvature types,

$$R_s = \frac{\int_{r_a}^{r_b} r^2 (P_N - P_T) dr}{\int_{r_a}^{r_b} r (P_N - P_T) dr} \quad (4)$$

and

$$S_e = \int_{r_a}^{r_b} \rho(r) \ln \frac{\rho(r)}{\rho_0} dr, \quad (5)$$

to obtain surface of tension and excess entropy of the interface, respectively, where ρ_0 is the overall density of the system and $r_{a,b}$ are the radial distances beginning in state a and ending in state b .

Curvature	$R_s(\text{integration})$	$R_c(\text{local})$	$\sigma_s(\text{integration})$	$\sigma_s(\text{local})$
Convex	3.94	4.54	0.037	0.054
Concave	3.84	-5.68	-0.085	-0.065

TABLE III: Values for the surface of tension, radius of surface curvature, and surface tension for convex and concave case for $T^* = 0.3$ $\rho^* = 1.17$, comparing values obtained from integration of pressure profiles to data obtained from local curvature fitting. (Note: Surface of tension R_s and radius of curvature R_c are not correlated physically.)

In our case, data collection is taken from the center of the cluster, so the integral S_e is taken from $r_a = 0$. Excess entropy S_e across the interface is negative in the convex case and positive in the concave case, which provide a measure of the surface tension at different regions of the interface and serves as a driving force for interface coarsening.

The general way to compute the surface tension for a fluid system is from the integration of the pressure profile,

$$\sigma_s = \int_0^\infty \left(\frac{r}{R_s} \right)^2 (P_N - P_T) dr, \quad (6)$$

where R_s is taken as the surface of tension and σ_s from integration of the pressure profiles can also be checked against the values obtained from the local curvature estimation, detailed in the next section. Some data for each curvature case are presented in Table III.

The surface tension as an excess free energy is related to the excess entropy via $\sigma_s = -S_e T$, as the excess energy can be neglected due to small density change in the interfacial region [13]. Because the surfaces sampled to obtain the pressure profiles is larger than that of the entropy calculation, the excess surface free energy is scaled down proportionally to the S_e interface. The excess entropy S_e in the convex case is $S_e(\text{convex}) = -0.076$, while $S_e(\text{concave}) = 0.20$ at $T^* = 0.3$, which compare well with $\sigma_s(\text{convex}) = 0.054$ and $\sigma_s(\text{concave}) = -0.065$ from Table III.

After the initial quenching to the liquid-liquid phase separation in the supercooled region, the coarsening kinetics is driven by the reduction of the surface tension. Given the complex morphology of the interfaces, our curvature dependent surface tension calculations may present a concrete method for the calculation of viscosity as a function of temperature.

IV. TEMPERATURE DEPENDENT VISCOSITY

A hallmark of the glass transition is the exponential growth of the viscosity as the temperature is lowered in the supercooled region [14]. Due to the many order of magnitudes difference between

the viscosity near the melting temperature and the glass transition temperature, the traditional method to compute the viscosity, such as the Green-Kubo method, can't be used across the whole temperature range due to the slow dynamics as the viscosity becomes many orders of magnitude larger than that of a normal liquid.

To overcome this limitation, Yip and coworkers developed a Markov network model to calculate viscosity for slow dynamical systems [15]. The model utilizes a variation of the Green-Kubo theory that describes stress relaxation by a Markov network of nodes. Each node contains a collection of particles called basin i with its own inherent stress

$$\sigma_i = \frac{1}{\Omega} \langle -Nk_B T \mathbf{I} + \sum_{n=1}^N \mathbf{x}_n \otimes \partial_{\mathbf{x}_n} V \rangle_i, \quad (7)$$

where \mathbf{I} is the 3x3 identity matrix. The two terms of the thermal average $\langle \rangle_i$ are the kinetic and virial components of stress for particles within each basin. The likelihood of a particle leaving basin i for basin j can be defined by the transition rate

$$a_{ij} = v_0 e^{-\frac{q_{ij}}{k_B T}}, \quad (8)$$

with v_0 being the trial frequency and q_{ij} the activation barrier. Assuming that the averaged stress for each basin is a Markovian process, the shear stress time correlation function $\langle \sigma(t) \sigma(t + \tau) \rangle$ used for viscosity calculations within the linear response theory can be substituted by a shear stress average over each basin, such that

$$\sigma(T) = \sum_i \sigma_i p_i(t), \quad (9)$$

where $p_i(t)$ is a state-residence function for each basin, equal to one if the system is in basin i at time t , and zero otherwise. The Green-Kubo viscosity expression can be transformed as

$$\eta(T) = \frac{\Omega}{k_B T} \int_0^\infty d\tau \langle \sigma(t) \sigma(t + \tau) \rangle = \frac{\Omega}{k_B T} \sum_i P_i \sigma_i \frac{1}{a_i} (\mathbf{A}(\omega = 0^+)^{-1} \sigma)_i, \quad (10)$$

where Ω is the volume, P_i the probability of belonging to basin i , σ_i the shear stress of basin i , a_i the transition rate to basin i . $(\mathbf{A}(\omega = 0^+)^{-1} \sigma)_i = \sum_j (\mathbf{A}(\omega = 0^+)^{-1})_{ij} \sigma_j$ is the propagator matrix between basin i and all others. The propagator matrix overcomes the need for a shear stress time correlation function calculation of the whole system, as the slow dynamics of the system make

averaging over each basin within the system a good approximation.

In their application of the Markov network model to the Kob-Andersen model, they used the inherent structures of the potential energy surface as a starting point for various temperature sampling of different basins of the super-cooled system. A crossover from an essentially Arrhenius scaling behavior at high temperatures to a low-temperature behavior that is clearly super-Arrhenius is observed for the Kob-Andersen model [15]. In the glass transition temperature region thousands of basins are needed for the sampling which makes the physical interpretation difficult.

In our case, the liquid-liquid phase separation picture naturally leads to two different kinds of basins at near equilibrium condition. The coarsening kinetics, which governs the particles transitions between different domains, will be an activated process and the activation energy can be measured by the surface tension between domains. If there are only two basins(domains) at quasi-equilibrium, then $P_1 = P_2 = 1/2$, $\sigma_1 = -\sigma_2 = \sigma_0$, and $a_{12} = a_{21} = v_0 \exp(-Q/k_B T)$, then Eq.(10) reduced to

$$\eta(T) = \frac{\Omega}{k_B T} \sigma_0^2 v_0^{-1} e^{\frac{Q}{k_B T}}, \quad (11)$$

where Q is the activation energy for particles transition between two basins, v_0 the frequency at which particles switch basins.

From our simulations the shear stress between two liquid states are equal and opposite, then Eq. 11 will become

$$\eta(T) = \frac{\Omega}{k_B T} \sigma_0^2 v_0^{-1} e^{\frac{\phi}{k_B T}}, \quad (12)$$

where $Q = \phi$ is the summation of the local surface tension of the liquid-liquid interface times the corresponding surface area, namely the total interfacial free energy. The surface tension calculated in the previous section for positive and negative curvatures can act as constructive and destructive interference, which provides a physical mechanism for the slow coarsening kinetics. In the previous section, the surface tension is calculated using the pressure profile at the interface, but this is a time-consuming process due to the long average of the pressure profile calculations. As the system is nearly at mechanical equilibrium, the Laplace equation can be used for the calculation of the surface tension and it is demonstrated in Table III that the Laplace equation calculation leads to essentially the same result from the pressure profile calculation.

Therefore, a per-particle local curvature is calculated for all interfacial particles in the system

N	N_i	$\sum_i \frac{a_i}{\kappa_i}$	$\overline{\kappa_i}$
8000	1051	270	0.067
15625	1625	262	0.05
19683	3470	271	0.031

(a) $T^* = 0.36$

N	N_i	$\sum_i \frac{a_i}{\kappa_i}$	$\overline{\kappa_i}$
8000	941	232	0.084
15625	2208	241	0.070
19683	3343	249	0.033

(b) $T^* = 0.38$

TABLE IV: Surface tension as a function of system size. $\sum_i \frac{a_i}{\kappa_i}$ is independent of N , while N_i , the number of interfacial particles, increases the mean curvature $\overline{\kappa_i}$ decreases. As the system size increases, regions of negative and positive curvature both increase (Fig. 8), the the final $\sum_i \frac{a_i}{\kappa_i}$ remains as a constant within statistical error.

and the activation energy of the whole interface is

$$\phi = \frac{1}{2} \Delta P \sum_i \frac{a_i}{\kappa_i}, \quad (13)$$

where ΔP is the difference in normal pressures between the two thermodynamic states, $a = \pi r^2$ the surface area of interfacial particles, and κ_i the local curvature of interfacial particle i . This local surface tension approach requires an accurate representation of local curvature, which is obtained by generating a surface using opposite-state neighbor lists of interfacial particles. One may also use the log-likelihood from PC space to find interfacial particles, detailed in appendix A.

To ensure that the calculation of interfacial free energy, particularly $\sum_i \frac{a_i}{\kappa_i}$, is independent of system size, viscosity was calculated following Eq.12 for sizes $N = [8000, 15625, 20000]$. The summation of the interfacial surface area times the inverse curvature, $\sum_i \frac{a_i}{\kappa_i}$, is independent of system size N as shown in Table IV and in Figure Fig. 8 at $T^* = 0.36$.

Finite box size effects at lower N cause single cluster nucleation with high curvature. As system size grows, mean curvature $\overline{\kappa_i}$ decreases as regions of negative curvature increase and both liquid states become bi-continuous as seen in Fig. 8. For this reason, interfacial free energy remains a constant as a function of system size.

Systems within the temperature range $T^* = [0.5, 0.52, 0.55]$ are still below the liquid-liquid transition line at $\rho^* = 1.12$ but above the mode-coupling temperature $T^* = 0.435$, hence their viscosities can be estimated using the Markov Network Model (Eq.12) and the conventional Green-Kubo method. The difference between these values is then adjusted by setting the trial frequency ν_0 , which is then used for all other temperatures. In conjunction with homogeneous liquid viscosities at $T^* = 1.0, 0.8$, the viscosities computed using our model are shown in Fig. 9.

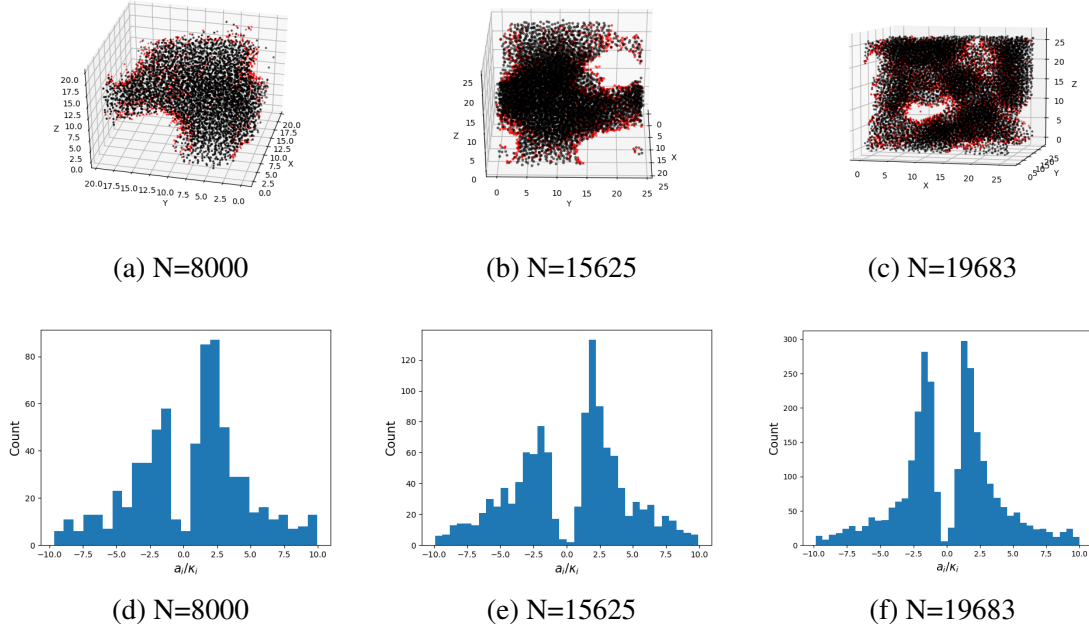


Fig. 8: (a-c) Configuration space displaying liquid particles belonging to one state (black) against the interfacial particles generated to represent their surface (red) at $T^* = 0.36, \rho^* = 1.12$ for $N = 8000, 15625, 19683$. Histograms (d-f) of $\frac{a_i}{K_i}$ from Eq. 13 demonstrate that as system size increase, regions of positive and negative curvatures scaled by local surface area increase. This shift allows for consistent interfacial free energy values as N increases.

T^*	0.36	0.38	0.4	0.43	0.46	0.5	0.52	0.55
ΔP^*	0.14	0.12	0.11	0.091	0.07	0.062	0.06	0.05
$\sum_i \frac{a_i}{K_i}$	265	241	162	124	114	109	104	113

TABLE V: Interfacial free energy and pressure difference of liquid states for $\rho^* = 1.12$ systems used to construct the reduced viscosity curve. The trial frequency $\nu_0^{-1} = 10s$ used at each temperature T^* is the one used to match Green-Kubo data from $T^* = [0.5, 0.52, 0.55]$. Shear stress σ_0 for each system is of the order 10^{-3} in reduced pressure unit, and the dimensions of the simulation box is 24 reduced units. The average area a occupied by each particle along the surface is $a = \pi r^2 = \pi(0.98)^2 = 3.015$ estimated from the bulk density, which doesn't vary as a function of temperature. Using these data and Eq.12 one can construct Fig. 9.

V. CONCLUDING REMARKS

Using the WCN as an order parameter, we have reproduced the gas-liquid binodal line and successfully extended the calculation to liquid-liquid binodal and its critical temperature for the Kob-Andersen model. There exists clear thermodynamic evidence of two coexisting liquid states from their pressure and density profiles. Coexistence densities of liquid states quenched at dif-

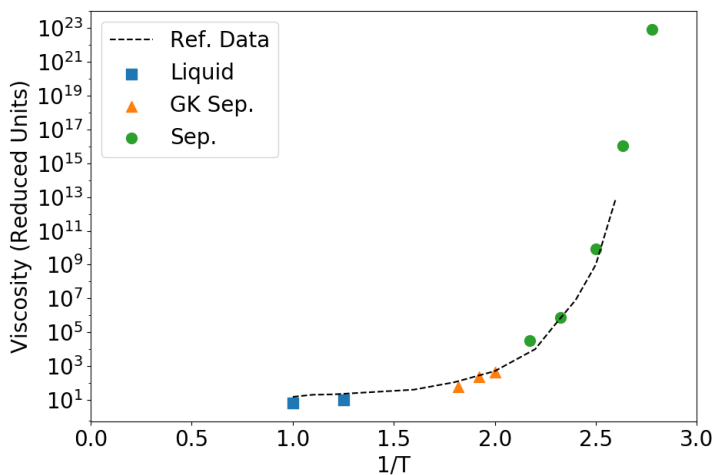


Fig. 9: Viscosity computed using the Markov Network Model(MNM) from Eq.(12). Viscosity values where Green-Kubo is still reliable within the liquid-liquid binodal are depicted by triangles. These systems are used to estimate the trial frequency ν_0 . Homogeneous liquid ones are denoted by squares, and those below the temperature limit of Green-Kubo where only MNM is reliable are shown by circles. The dashed line is from the data in Ref.[15], where MNM is used with thousands of inherent structures as basins.

ferent bulk densities obey the level rule at a particular temperature, a strong indication of local thermodynamic equilibrium.

As temperature decreases to the glass transition region, the Markov Network Model is adopted for the computation of temperature dependent viscosity using the liquid-liquid phase separation picture. Almost 16 order of magnitudes increase in viscosity over a temperature range 0.55 to 0.36, clearly indicating super-Arrhenius behavior. The physical mechanism for such a drastic dynamical slowing down is due to the coarsening kinetics of the liquid-liquid phase separation as indicated from the Markov Network Model calculations.

Application to the ST2 water model [16] also indicates liquid-liquid phase separation as demonstrated from other methods indirectly [17–19], the temperature dependent viscosity calculations are under way. If super-Arrhenius behavior is also observed, then liquid-liquid phase separation mechanism may provide a simple picture for the understanding of glass transitions in general. Naturally, it will be interesting to explore other salient features of glass transition as shown from other glass transition studies [14] within the current liquid-liquid phase separation picture.

VI. ACKNOWLEDGEMENT

This work is supported by the Division of Chemical and Biological Sciences, Office of Basic Energy Sciences, U.S. Department of Energy, under Contact No. DE-AC02-07CH11358 with Iowa State University.

Appendix A: Local Curvature Calculations

Two approaches are utilized to estimate the local surface of interfacial particles for the local curvature estimation to make sure reliable results are obtained consistently.

The first approach utilizes local neighbor lists for interfacial particles, gathered under the criterion that 70% of a particle's neighbors belong to the other state. Midpoints between each of these tagged particles are made with its neighbors belonging to the other state, generating surfaces with many more points to sample than just the particles along the surface, which is limited by density. This approach creates a surface with many more particles to sample along the liquid-liquid interface, allowing for more precise fitting of local surfaces.

The second approach uses the log-likelihood information from the PC space to determine which particles have the highest probability of belonging to either state. The issue with this approach is that K-means clustering in the PC space is non-deterministic so the particles assigned to the surface may vary, and the number of particles collected using this approach is far fewer than the prior method. Additionally, the log-likelihood gap between states becomes smaller as the liquid states become more thermodynamically similar close to T_c^* , therefore making the first approach more reliable and the method used in all analysis.

Once a local surface containing an interfacial particle is constructed, the following procedure leads to the local curvature:

1. Generate surface point neighbor lists (from PC's or neighbor information).
2. Points and their neighbors are fit to 2D quadric equation $F(x, y, z) = ax^2 + by^2 + cz^2 + 2exy + 2fyx + 2gxz + 2lx + 2my + 2nz + d = 0$ using the least squares method. We do not wish to calculate the nearest point on the fitted plane to the surface point of interest. Instead, we assume $F(P) = 0$, with P being the surface point of interest.
3. Using coefficients from fitting, compute first fundamentals of $F(x, y, z)$,

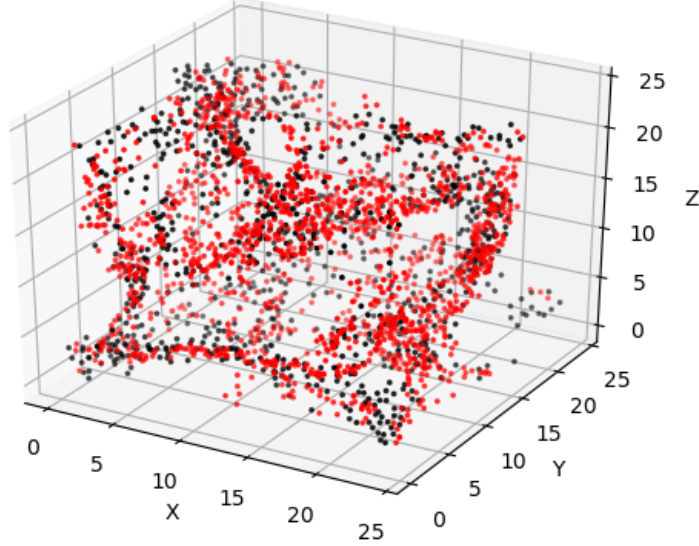


Fig. 10: Comparison of methods for construction of local surface that embeds an interfacial particle, using neighbor lists (red) and using PC log-likelihood (black). Log-likelihood gets more inconsistent closer to the liquid-liquid binodal line, and so neighbor lists are more reliable for local surface construction.

$$E = 1 + \frac{F_x^2}{F_z^2}, \quad F = \frac{F_x F_y}{F_z^2}, \quad G = 1 + \frac{F_y^2}{F_z^2} \quad (\text{A1})$$

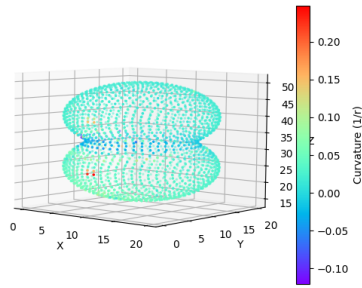
and the second fundamentals

$$L = \frac{1}{F_z^2 |\nabla F|} \begin{vmatrix} F_{xx} & F_{xz} & F_x \\ F_{zx} & F_{zz} & F_z \\ F_x & F_z & 0 \end{vmatrix}, \quad M = \frac{1}{F_z^2 |\nabla F|} \begin{vmatrix} F_{xy} & F_{yz} & F_y \\ F_{zx} & F_{zz} & F_z \\ F_x & F_z & 0 \end{vmatrix}, \quad N = \frac{1}{F_z^2 |\nabla F|} \begin{vmatrix} F_{yy} & F_{yz} & F_y \\ F_{zy} & F_{zz} & F_z \\ F_y & F_z & 0 \end{vmatrix}. \quad (\text{A2})$$

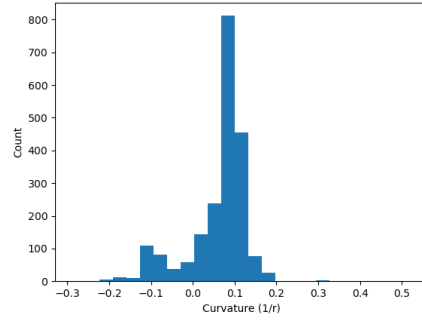
Once the fundamentals have been computed, the principle curvatures may be determined by constructing the matrices

$$A = \begin{bmatrix} L & M \\ M & N \end{bmatrix}, \quad B = \begin{bmatrix} E & F \\ F & G \end{bmatrix} \quad (\text{A3})$$

and the eigenvalues of $B^{-1}A$ correspond to k_1, k_2 , with mean curvature $H = (k_1 + k_2)/2$.

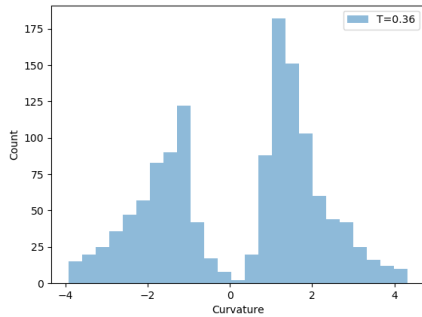


(a) Diatomic

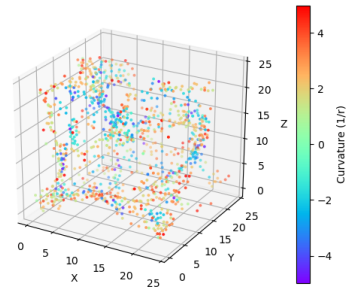


(b) Histogram

Fig. 11: (a) Curvature estimation of a diatomic molecule using 2D quadric plane fit and (b) histogram of curvature values. The hemispheres of the diatomic have radius $r = 10$, resulting in curvature values consistent with $1/r$. This verification of accuracy of a surface with both convex and concave curvature allows us to extend it to the Kob-Andersen case.



(a) Histogram data



(b) Color mapping of surface particles

Fig. 12: Curvature data collected using PC space log-likelihood to detect interfacial particles of $T^* = 0.36$, $\rho^* = 1.12$ Kob-Andersen system. 2D quadric plane fit was used to calculate local curvature for each interfacial particle.

To test our algorithm of the implementation the curvatures of a perfect sphere with $r = 1$ and a diatomic molecule with atomic radius $r = 10$ with bond length=2. The expected curvature value for the sphere and hemispheres of the diatomic are given by the relation $\kappa = \frac{1}{r}$. Figure Fig. 11 shows the diatomic curvature estimations. Fig. 12 shows the curvature distribution of interfacial particles at a particular liquid-liquid phase separation condition.

[1] Viet Nguyen and Xueyu Song. A general classification scheme of detecting spatial and dynamical heterogeneities in super-cooled liquids. *arXiv.2203.11989*, 2022.

- [2] Viet Nguyen and Xueyu Song. Automated characterization of spatial and dynamical heterogeneity in supercooled liquids via implementation of machine learning. *Journal of Physics: Condensed Matter*, 35(46):465401, 2023.
- [3] Walter Kob and Hans C. Andersen. Testing mode-coupling theory for a supercooled binary lennard-jones mixture i: The van hove correlation function. *Phys. Rev. E*, 51:4626–4641, 1995.
- [4] Walter Kob and Hans C. Andersen. Scaling behavior in the β -relaxation regime of a supercooled lennard-jones mixture. *Phys. Rev. Lett.*, 73:1376–1379, 1994.
- [5] S. S. Ashwin, Gautam I. Menon, and Srikanth Sastry. The glass transition and liquid-gas spinodal boundaries of metastable liquids. *Europhysics Letters*, 75(6):922, 2006.
- [6] Srikanth Sastry. Liquid limits: Glass transition and liquid-gas spinodal boundaries of metastable liquids. *Phys. Rev. Lett.*, 85:590–593, 2000.
- [7] Vincent Testard, Ludovic Berthier, and Walter Kob. Intermittent dynamics and logarithmic domain growth during the spinodal decomposition of a glass-forming liquid. *The Journal of Chemical Physics*, 140(16):164502, 2014.
- [8] Hiroshi Watanabe, Nobuyasu Ito, and Chin-Kun Hu. Phase diagram and universality of the lennard-jones gas-liquid system. *The Journal of Chemical Physics*, 136(20):204102, 2012.
- [9] Aidan P. Thompson, H. Metin Aktulga, Richard Berger, Dan S. Bolintineanu, W. Michael Brown, Paul S. Crozier, Pieter J. in’t Veld, Axel Kohlmeyer, Stan G. Moore, Trung Dac Nguyen, Ray Shan, Mark J. Stevens, Julien Tranchida, Christian Trott, and Steven J. Plimpton. Lammmps - a flexible simulation tool for particle-based materials modeling at the atomic, meso, and continuum scales. *Computer Physics Communications*, 271:108171, 2022.
- [10] J. S. Rowlinson and B. Widom. *Molecular theory of capillarity*. Dover, Oxford, Oxfordshire, 1982.
- [11] Daan Frenkel and Berend Smit. *Understanding molecular simulation: from algorithms to applications*. Academic, 2nd ed. edition, 2002.
- [12] Deepti Ballal, Qing Lu, Muralikrishna Raju, and Xueyu Song. Studying vapor-liquid transition using a generalized ensemble. *The Journal of Chemical Physics*, 151(13):134108, 2019.
- [13] K. G. S. H. Gunawardana and Xueyu Song. Theoretical prediction of crystallization kinetics of a supercooled lennard-jones fluid. *The Journal of chemical physics*, 148(20):204506, 2018.
- [14] P. G. Wolynes and Vassiliy Lubchenko. *Structural glasses and supercooled liquids : theory, experiment, and applications*. Wiley, Hoboken, New Jersey, 2012.
- [15] Ju Li, Akihiro Kushima, Jacob Eapen, Xi Lin, Xiaofeng Qian, John C. Mauro, Phong Diep, and Sidney

- Yip. Computing the viscosity of supercooled liquids: Markov network model. *PLOS ONE*, 6:1–7, 2011.
- [16] Frank H. Stillinger and Aneesur Rahman. Improved simulation of liquid water by molecular dynamics. *The Journal of Chemical Physics*, 60(4):1545–1557, 1974.
- [17] Francesco Sciortino, Ivan Saika-Voivod, and Peter H Poole. Study of the st2 model of water close to the liquid–liquid critical point. *Physical Chemistry Chemical Physics*, 13(44):19759–19764, 2011.
- [18] Takuma Yagasaki, Masakazu Matsumoto, and Hideki Tanaka. Spontaneous liquid-liquid phase separation of water. *Phys. Rev. E*, 89:020301, 2014.
- [19] Yang Liu, Athanassios Z. Panagiotopoulos, and Pablo G. Debenedetti. Low-temperature fluid-phase behavior of st2 water. *The Journal of Chemical Physics*, 131(10):104508, 2009.